scientific reports

Check for updates

OPEN

Discrete time domain modeling and design of current mode controlled flyback LED driver

Marn-Go Kim

In this paper, modeling for a current mode controlled (CMC) flyback LED driver with a stabilizing ramp is performed in a step-by-step procedure. Discrete time state equations for the system are derived and linearized with respect to a steady-state operating point. At this operating point, the switching control law, the condition that determines the duty ratio, is also linearized. In the next step, a closed-loop system model is derived by combining the two models of the flyback driver and the switching control law. The root locus analysis in the z-plane is used to investigate the characteristics of the combined linearized system and obtain design guidelines for feedback loops. The feasibility of the proposed design is confirmed through the experimental results for the CMC flyback LED driver.

In recent years, light emitting diode (LED) lighting becomes increasingly popular owing to the advantages of its high luminous efficacy, environmental friendliness, long lifespan, and fast response[1]. The brightness of an LED is mainly controlled by the forward current of the LED supplied by a current converter. Due to the manufacturing tolerance of forward voltage and internal resistance of individual LEDs, accurately controlling the forward current is an important issue. Therefore, it is necessary to control the current to get the brightness of the LEDs precisely[2–4]. A lot of work has been done recently for the applications of power LEDs, including rectification with a high-power factor[5–11] and current balancing between LED strings[12–14].

Several small-signal model approaches have been attempted to characterize current-mode controlled converters. A low-frequency average approach was proposed in[15]. The modulator model is derived from the perturbation of an equation for the average inductor current in steady-state. This model has gained wide acceptance owing to its simplicity. However, one general limitation of the averaging model is its inability to predict high-frequency small-signal dynamics near half of the switching frequency. Discrete-time models[16] can accurately predict the response at high frequencies, but provide little design insight due to their complex formulas based on numerical techniques. So far, when modeling the behavior of the modulator, it has been assumed that the operation of the control signal v_c in the output feedback loop is much slower than the switching operation. This approach is suitable for voltage regulating converters because a low-pass filter is added in the output.

Current control is required to accurately maintain the brightness of the LEDs. The control signal v_c in the output feedback loop of the current controlled converter is fast. Therefore, it cannot be regarded as a constant over a switching period. This is because a low-pass filter for the feedback output current is not necessarily required. In the current regulating converter, the instantaneous control signal v_c in the output feedback loop must be used to model the behavior of the modulator. In order to improve the characteristics of the LED driver, an optimal design of the circuits in the feedback loops is required. However, very little research has been done in this area[17–21].

In this paper, modeling and analysis of the CMC flyback LED driver shown in Fig. 1 is performed using a systematic modeling technique[22–25]. The root locus analysis in the z-plane is utilized to derive the stability boundary as a function of D. Design guidelines for feedback loops such as stabilization ramp slope and integrator gain are presented in a step-by-step process. In particular, this paper reveals for the first time that the proportional gain of the proportional-integral (PI) error amplifier in the output current feedback loop is not related to the dynamic characteristics of the CMC flyback LED driver. This is because, when the switch is on, the output current of the flyback converter is 0, so the slope change of the control signal by the output current does not occur. The validity of the proposed analysis and design is confirmed through transient response experiments.

School of Electrical Engineering, Pukyong National University, Busan, Republic of Korea. email: mgkim@pknu.ac.kr

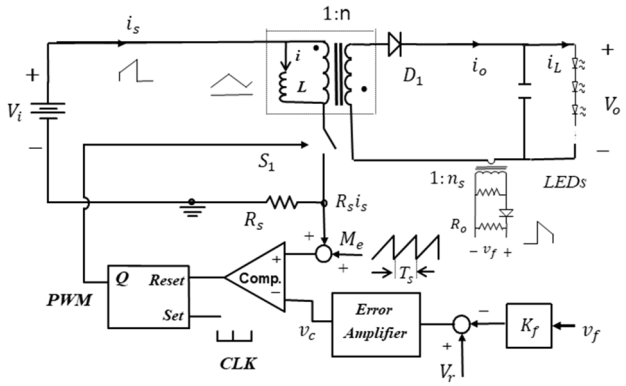

Figure 1. Constant-frequency CMC flyback LED driver with stabilization ramp.

Modeling of CMC flyback LED driver

The following assumptions are utilized to perform the discrete time domain model:

- The flyback converter is operating in continuous conduction mode (CCM),
- All switches are ideal,
- The loading effect on the power stage by the feedback loop is negligible,
- The input and output voltages are DC.

Discrete-time state equations. The switch-on state is initiated when a clock signal is applied to the Set input of the PWM modulator. The switched-on state ends when the sum of the stabilization ramp M_e and the inductor current sense signal $R_s i_s$ reaches the control signal v_c.

The duty ratio d_k is determined when the two comparator inputs are equal as follows

$$R_s(i_k + m_1 T_s d_k) + M_e T_s d_k = v_c|_{t=t_k+T_s d_k} \tag{1}$$

where i_k is the primary inductor current at the beginning of the k-th cycle, M_e is the external ramp slope added for stabilization, and m_1 is the positive slope of inductor current when the power switch is ON.

In Fig. 2, the inductor current can be expressed in the discrete time domain by the equation

$$i_{k+1} = i_k + m_1 T_s d_k - m_2 T_s (1 - d_k) \tag{2}$$

where i_{k+1} is the primary inductor current at the end of the k-th cycle, and m_2 is the negative slope of inductor current when the power switch is OFF.

As the error amplifier circuit of the output current feedback loop, a PI compensator is used as shown in Fig. 3. The capacitor voltage of the error amplifier can be written in the discrete time domain by the equation

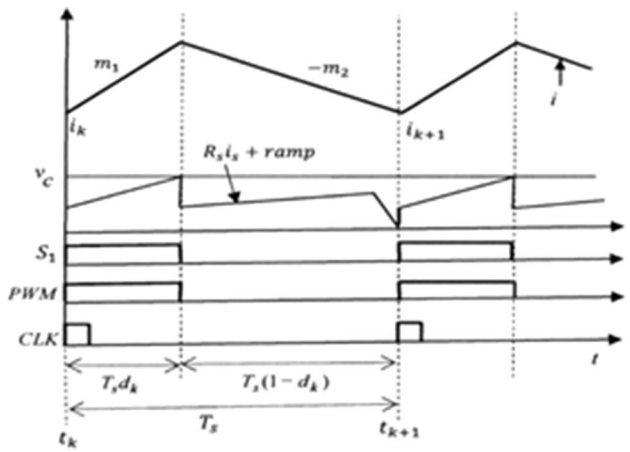

Figure 2. Key typical waveforms of Fig. 1.

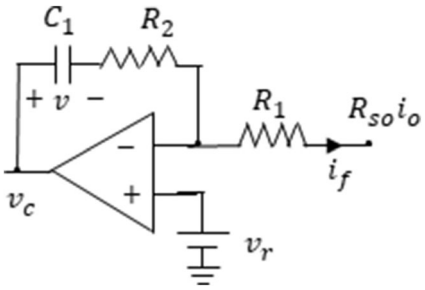

Figure 3. PI error amplifier in the output feedback loop.

$$\begin{aligned} v_{k+1} &= v_k + \frac{1}{C_1}\int_{t_k}^{t_{k+1}} \frac{(v_r - R_{so}i_o)}{R_1}dt \\ &= v_k + \frac{R_{so}T_s}{R_1C_1}\left(\frac{v_r}{R_{so}} - i_{avg,k}\right) \end{aligned} \tag{3}$$

where $R_{so} = \frac{R_oK_f}{n_s}$, $i_{avg,k} = \frac{1}{T_s}\int_{t_k}^{t_{k+1}} i_o dt$, n_s is the turns ratio of output current sense transformer, K_f is the output current feedback gain and R_o is the output current sense resistor.$i_{avg,k}$, which is the average output current of k-th cycle, can be calculated as

$$i_{avg,k} = \frac{1}{n}\{i_k + m_1T_sd_k - m_2\frac{T_s(1-d_k)}{2}\}\cdot(1-d_k) \tag{4}$$

where n is the turns ratio of the flyback transformer.

Since i_o is 0 for $t_k \le t < t_k + T_sd_k$, the control signal v_c at the moment of switching can be represented as

$$\begin{aligned} v_c|_{t=t_k+T_sd_k} &= v_r + \frac{R_2}{R_1}v_r + v_k + \frac{1}{C_1}\int_{t_k}^{t_k+T_sd_k}\frac{v_r}{R_1}\mathrm{dt} \\ &= v_r + k_p\cdot v_r + v_k + k_iT_sd_k\cdot v_r \end{aligned} \tag{5}$$

where the P gain k_p is $\frac{R_2}{R_1}$ and the I gain k_i is $\frac{1}{R_1C_1}$. When v_r is constant, the slope of the control signal at the switching moment is not affected by k_p.

Equilibrium state. Setting $m_1 = M_1$, $m_2 = M_2$,$d_k = D$,$i_{k+1} = i_k = I$, $v_{k+1} = v_k = V$, $i_{avg,k} = I_{avg}$ $i_{avg,k} = I_{avg}$ $i_{avg,k} = I_{avg}$, and $v_r = V_r$, the following steady-state conditions can be obtained from (2) and (3):

$$M_1T_sD = M_2T_s(1-D) \tag{6a}$$

$$I_{avg} = V_r/R_{so} \tag{6b}$$

where $D = \frac{V_o/n}{V_i+V_o/n}$, $M_1 = V_i/L$ and $M_2 = \frac{V_o/n}{L}$.

Using (4), the average output current I_{avg} at equilibrium state can be written as

$$I_{avg} = \frac{1}{n}\left[I + M_1T_sD - \frac{M_2T_s(1-D)}{2}\right](1-D) = \frac{V_r}{R_{so}} \tag{7}$$

Linearization. Equations (2) and (3) can be expressed concisely as

$$i_{k+1} = f_1[i_k, v_k, d_k, v_r] \tag{8a}$$

$$v_{k+1} = f_2[i_k, v_k, d_k, v_r] \tag{8b}$$

The switching control law can also be expressed from Eqs. (1) and (5) as

$$f_3[i_k, v_k, d_k, v_r] = 0 \tag{9}$$

Linearizing Eq. (8a) with respect to the operating point gives

$$\delta i_{k+1} = \frac{\partial f_1}{\partial i_k}|_*\cdot\delta i_k + \frac{\partial f_1}{\partial v_k}|_*\cdot\delta v_k + \frac{\partial f_1}{\partial d_k}|_*\cdot\delta d_k + \frac{\partial f_1}{\partial v_r}|_*\cdot\delta v_r \tag{10}$$

where
$\frac{\partial f_1}{\partial i_k}|_* = 1, \frac{\partial f_1}{\partial v_k}|_* = 0, \frac{\partial f_1}{\partial d_k}|_* = (M_1 + M_2)T_s = \frac{V_i + V_o/n}{f_s L}$,
$\frac{\partial f_1}{\partial v_r}|_* = 0$.
Using steady-state conditions, linearizing Eq. (8b) with respect to the operating point also gives

$$\delta v_{k+1} = \frac{\partial f_2}{\partial i_k}|_* \cdot \delta i_k + \frac{\partial f_2}{\partial v_k}|_* \cdot \delta v_k + \frac{\partial f_2}{\partial d_k}|_* \cdot \delta d_k + \frac{\partial f_2}{\partial v_r}|_* \cdot \delta v_r \tag{11}$$

where
$\frac{\partial f_2}{\partial i_k}|_* = -k_i T_s R_{so}(1-D)/n, \frac{\partial f_2}{\partial v_k}|_* = 1$,
$\frac{\partial f_2}{\partial d_k}|_* = -k_i T_s \cdot \frac{R_{so}}{n}[\left(M_1 T_s + \frac{M_2 T_s}{2}\right) \cdot (1-D) - \frac{V_r}{R_{so}} \cdot \frac{n}{1-D}]$,
$\frac{\partial f_2}{\partial v_r}|_* = k_i T_s$.
Linearizing the switching control law in Eq. (9) can be derived as

$$\frac{\partial f_3}{\partial i_k}|_* \cdot \delta i_k + \frac{\partial f_3}{\partial v_k}|_* \cdot \delta v_k + \frac{\partial f_3}{\partial d_k}|_* \cdot \delta d_k + \frac{\partial f_3}{\partial v_r}|_* \cdot \delta v_r = 0 \tag{12}$$

where
$\frac{\partial f_3}{\partial i_k}|_* = 1, \frac{\partial f_3}{\partial v_k}|_* = -\frac{1}{R_s}, \frac{\partial f_3}{\partial d_k}|_* = M_1 T_s + \frac{M_e T_s}{R_s} - K_i T_s \cdot \frac{V_r}{R_s}$
$\frac{\partial f_3}{\partial v_r}|_* = -(1 + k_p + k_i T_s D)/R_s$.

Combination of state equations and control law. Equation (12) can be used to derive the following form for the linearized control law:

$$\delta d_k = -K_1 \cdot \delta i_k - K_2 \cdot \delta v_k - K_3 \cdot \delta v_r \tag{13}$$

where
$K_1 = \frac{1}{M_1 T_s + \frac{M_e T_s}{R_s} - k_i T_s \cdot \frac{V_r}{R_s}}, K_2 = -\frac{K_1}{R_s}$, and

$$K_3 = -\frac{1 + k_p + k_i T_s D}{R_s} \cdot K_1$$

Substituting (13) into (10) and (11) yields the following closed-loop system:

$$\delta X_{k+1} = A \cdot \delta X_k + B \cdot \delta v_r \tag{14}$$

where $\delta X_{k+1} = [\delta i_{k+1} \delta v_{k+1}]^T$, $\delta X_k = [\delta i_k \delta v_k]^T$. $A = \begin{bmatrix} a_{11} & a_{12} \\ a_{21} & a_{22} \end{bmatrix}$, $B = \begin{bmatrix} b_1 \\ b_2 \end{bmatrix}$, $a_{11} = 1 - (M_1 + M_2)T_s \cdot K_1 = 1 - \frac{V_i + V_o/n}{fL} \cdot K_1$, $a_{12} = -(M_1 + M_2)T_s \cdot K_2 = \frac{V_i + V_o/n}{fL} \cdot \frac{K_1}{R_s}$, $a_{21} = -k_{ni} \cdot \frac{R_{so}}{n}(1-D) + k_{ni} \cdot \frac{R_{so}}{n}\left[\frac{V_i + 0.5V_o/n}{fL} \cdot (1-D) - \frac{V_r}{R_{so}} \cdot \frac{n}{1-D}\right] \cdot K_1$, $a_{22} = 1 - \frac{k_{ni}}{R_s} \cdot \frac{R_{so}}{n} \cdot [\frac{V_i + 0.5V_o/n}{fL} \cdot (1-D) - \frac{V_r}{R_{so}} \cdot \frac{n}{1-D}] \cdot K_1$, $b_1 = -(M_1 + M_2)T_s \cdot K_3 = \frac{V_i + V_o/n}{fL} \cdot \left(1 + k_p + k_{ni} D\right) \cdot \frac{K_1}{R_s}, b_2 = k_{ni} - \frac{k_{ni}}{R_s} \cdot \frac{R_{so}}{n} \cdot \left[\frac{V_i + 0.5V_o/n}{fL} \cdot (1-D) - \frac{V_r}{R_{so}} \cdot \frac{n}{1-D}\right] \cdot \left(1 + k_p + k_{ni} D\right) \cdot K_1$, $K_1 = \frac{1}{M_1 T_s} \cdot \frac{1}{1 + S_r - k_{ni} \cdot \frac{V_r}{R_s} \cdot \frac{1}{M_1 T_s}}$, $S_r = \frac{L M_e}{R_s V_o/n} \cdot \frac{D}{(1-D)} = S_{ro} \cdot \frac{D}{(1-D)} \mathrm{D} = \frac{V_o/n}{V_i + V_o/n} k_p = \frac{R_2}{R_1}$,

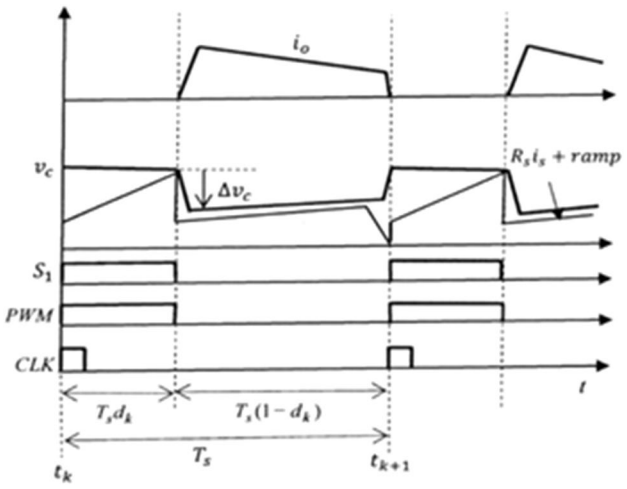

Figure 4. Effect of k_p on the control signal v_c: $\Delta v_c = k_p R_{so} i_o$.

$k_{ni} = k_i T_s = \frac{T_s}{R_1 C_1}$, $f_s = \frac{1}{T_s}$, $R_{so} = \frac{R_o K_f}{n_s}$. S_{ro} is the ratio of the external ramp slope to the off-time current slope multiplied by R_s.

Design guidelines

k_p independent of the location of the eigenvalues. In system Eq. (14), the terms of matrix A are independent of k_p. So k_p does not affect the characteristics of the system. Figure 4 shows the effect of k_p on the control signal v_c. When k_p is present, it causes a change in the control signal. Proportional gain k_p relates to the change of the control signal Δv_c when the switch is off, but does not affect the slope of the control signal when the switch is on. In other words, the small signal dynamics and stability related to the slope of the control signal at the switching moment are not affected by the resistor R_2. Therefore, it is desirable to remove R_2 from the error amplifier, resulting in $k_p = 0$. This is because a large k_p may cause the error amplifier to malfunction.

The eigenvalues of matrix A corresponding to the poles of the system are calculated to analyze the dynamics of the entire system. The eigenvalues of A are the solutions of

$$\boldsymbol{det}(\mathbf{zI} - \mathbf{A}) = 0 \tag{15}$$

where I is the unit matrix.

Selection of S_{ro}. S_{ro} Is the normalized slope of external ramp. As is well known, the current mode control is unstable in CCM when the duty cycle is greater than 0.5. A compensation ramp is added to avoid this problem. In the control strategy, the slope of the external compensation is constant. To ensure the stability of the control loop, the slope of the external ramp should be at least 50% of the downward slope of the inductor current[26]

$$S_{ro} \geq 0.5 \tag{16}$$

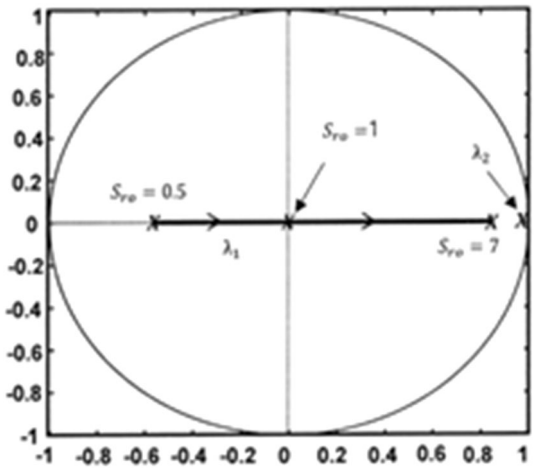

Figure 5. Root locus in the z-plane when varying S_{ro} for k_p=0, k_{ni}=0.003, and D = 0.75.

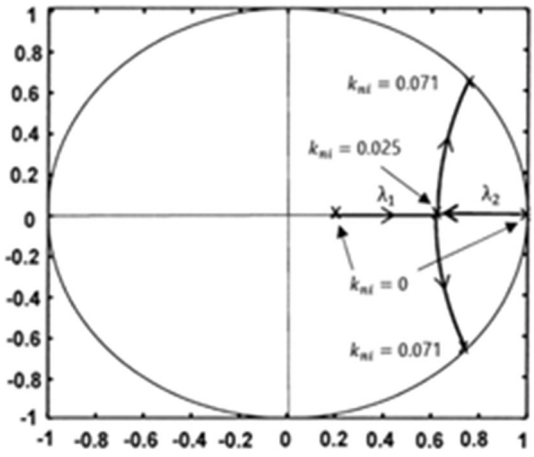

Figure 6. Root locus in the z-plane when varying k_{ni} for k_p=0, S_{ro} = 1.5 and D = 0.55.

The root locus obtained by varying the S_{ro} value for $k_p = 0$ and $k_{ni} = 0.003$ is shown in Fig. 5. As S_{ro} increases from 0.5 to 1, the transient response of inductor current which is dominated by λ_1 changes from underdamping to the fastest response. This is because the eigenvalue λ_1 shifts to the center of the unit circle. When S_{ro} is greater than 1, the transient response of inductor current is overdamped. Selecting S_{ro} slightly greater than 1 causes the closed-loop system to be slightly overdamped without oscillation. On the other hand, the eigenvalue λ_2, which dominates the dynamic performance of the slower integrator state, is fixed near the unit circle. Choosing an S_{ro} slightly greater than or equal to 1 can provide a good transient response.

Selection of k_{ni}. Next, the root locus is obtained by changing k_{ni} for $R_s = 0.25\Omega$, $R_{so} = 3\Omega$, $v_r = 2.5$V, $T_s = 10\mu$s, L $= 310\mu$H, $S_{ro} = 1.5$, n = 1, $V_o = 30$V, and D = 0.55. Figure 6 shows the root locus obtained by varying the integral gain k_{ni} value for $k_p = 0$. When the I gain k_{ni} of the error amplifier changes from 0 to 0.025, the system response changes from overdamping to critical damping. The system responds faster because the slower eigenvalue λ_2 shifts towards the center of the unit circle. When k_{ni} is greater than 0.025, the transient response is underdamped and oscillations occur. Choosing a k_{ni} greater than 0.071 makes the closed loop system unstable.

Figure 7 shows stability boundary and critical gain curve of k_{ni} as a function of D. When all eigenvalues of a system are within the unit circle, the stability of the system is assured. This region is when k_{ni} is between 0 and the stability boundary. Selecting an integral gain greater than the boundary can cause the system to be unstable. This unstable area is grayed out. It is recommended to design the integral gain so that the system response is critical damping. When the two poles coincide, i.e. λ_1=λ_2, the system response is critically damped. We can plot the critical gain with a dashed line between the underdamped and overdamped regions by using the condition

$$(a_{11} + a_{22})^2 - 4(a_{11}a_{22} - a_{12}a_{21}) = 0 \tag{17}$$

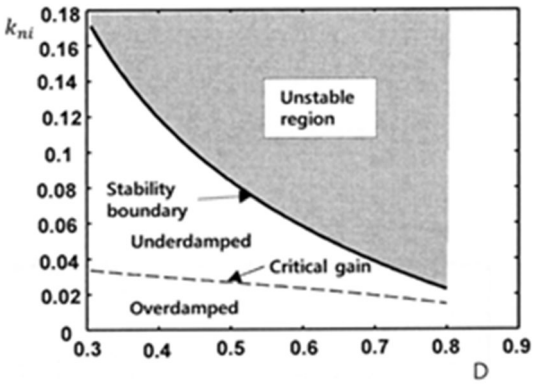

Figure 7. Theoretical stability boundary and critical gain curve of k_{ni} as a function of D when $k_p = 0$.

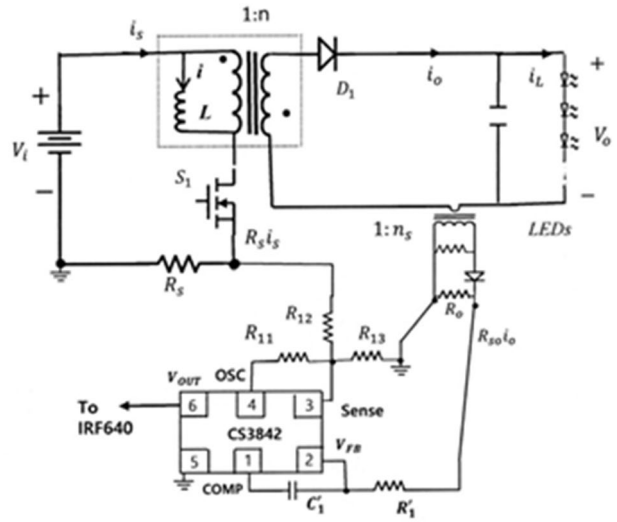

Figure 8. Experimental prototype circuit of CMC flyback LED driver with stabilization ramp.

f_s	100 kHz	$C_1^{'}$	47 nF
D	0.55	S_1	IRF640
L	310 μH	D_1	MBRF10100CT
R_s	0.25 Ω	LEDs	SZ5-W0-M0-00
V_o	30 V	Load current	833 mA
R_o	150 Ω	R_{11}	50 kΩ
n	1	R_{12}	10 kΩ
n_s	50	R_{13}	50 kΩ
K_f	1	V_i	25 V
S_{ro}	1.5	Control IC	CS3842

Table 1. Components and system parameters used in the experiment.

Experimental evaluation

For evaluation through experiments, a prototype converter circuit was implemented as shown in Fig. 8. The components and parameters of Fig. 8 are listed in Table 1. Switching is constant at 100 kHz frequency. CS3842 is used as the control IC. The output voltage is approximately 30 V (3.0 V × 10 LEDs in series). In the datasheet of CS3842, the OSC peak-to-peak swing ΔV is 1.8 V[27]. The rising slope of OSC is $M_e = \Delta V/T_s = 1.8 \times 10^5$. For the operating point and system parameters, S_{r0} is $\frac{LM_e}{R_s V_o} \times \frac{R_{12}}{R_{11}} = \frac{310X10^{-6} \times 1.8X10^5}{0.25 \times 30} \times \frac{R_{12}}{R_{11}} = 7.44 \times \frac{R_{12}}{R_{11}}$. To design S_{r0} to be 1.5, slightly greater than 1, the values of R_{11} and R_{12} are chosen to be 50 kΩ and 10 kΩ, respectively. In the datasheet[27], the Sense signal should be limited to within 1 V. The maximum value of OSC voltage is 2.8 V. If the maximum value of the primary-side inductor current is set to 3.5A, the maximum value of the Sense signal is $\max\left(\text{OSC}X\frac{1}{5} + R_s i_s\right)XSF = \left(2.8X\frac{1}{5} + 0.25X3.5\right)XSF = 1V$. So, SF is 0.7. In Fig. 8, the Sense signal can be derived as $\text{OSC} \cdot \frac{R_{12}R_{13}}{R_{12}+R_{13}}/(R_{11} + \frac{R_{12}R_{13}}{R_{12}+R_{13}}) + R_s i_s \cdot \frac{R_{11}R_{13}}{R_{11}+R_{13}}/(R_{12} + \frac{R_{11}R_{13}}{R_{11}+R_{13}})$. Therefore, $\frac{R_{11}R_{13}}{R_{11}+R_{13}}/(R_{12} + \frac{R_{11}R_{13}}{R_{11}+R_{13}}) = \text{SF} \approx 0.7$. Substituting $R_{11} = 50\text{k}\Omega$ and $R_{12} = 10\text{k}\Omega$ into this equation gives $R_{13} = 50\text{k}\Omega$.

When the integral gain k_{ni} is multiplied by the scale factor (SF), the characteristics of the real system become the same as the theoretical analysis[20]. So, the actual integral gain $k_{ni}^{'}$ in the output feedback loop becomes $k_{ni}XSF$. In the experimental circuit, the output signal of the error amplifier is reduced by 1/3 by the voltage divider resistors. So, the designed integral gain in the output feedback loop $k_{ni}^{'}$ is $\frac{1}{3} \times \frac{T_s}{R_1^{'}C_1^{'}}$. Setting $C_1^{'} = 47\text{nF}$ gives $k_{ni} = \frac{k_{ni}^{'}}{SF} = \frac{1}{0.714X3} \times \frac{10^{-5}}{R_1^{'}X47X10^{-9}} = \frac{0.0993X10^3}{R_1^{'}}$.

In the experiment, 10 LEDs were connected in series to provide a load voltage of about 30 V. Figure 9 shows a picture of the implementation hardware. As shown in Fig. 10, the LED current i_L, the output of the error amplifier COMP, and the transformer secondary current i_o are measured for the starting transient when the integral gain is changed. The overall response time is faster as the integral gain varies from 0.0083 to 0.027. An optimal transient response is measured when k_{ni} is 0.027, that is, near the point $\lambda_1 = \lambda_2$. By changing the integral gain to 0.055, the transient response of the system exhibits slight oscillations. Increasing k_{ni} to 0.1 results in an unstable system with pole locations outside the unit circle. At $k_{ni} = 0.1$, the pole positions in the z-plane are 0.9 ± j0.87. The z-plane pole positions are expressed as the s-plane pole positions as follows[28]: $z = e^{sT_s}|_{s=\sigma \pm jw} = e^{\sigma T_s}/\pm wT_s$ =1.25/±0.768. Since wT_s=0.768, the closed-loop oscillation frequency is $f_{osc} = \frac{0.768}{2\pi T_s} = 0.122f_s$. So, the oscillation

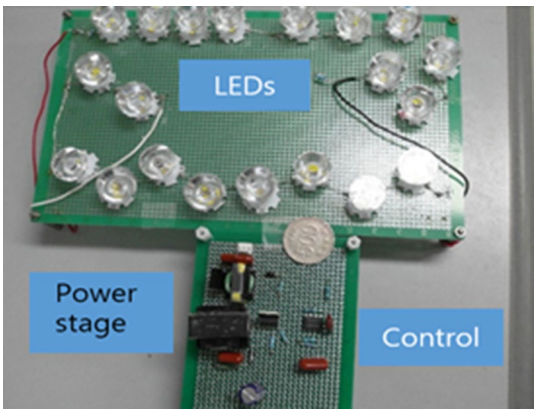

Figure 9. Photo of the experimental implementation.

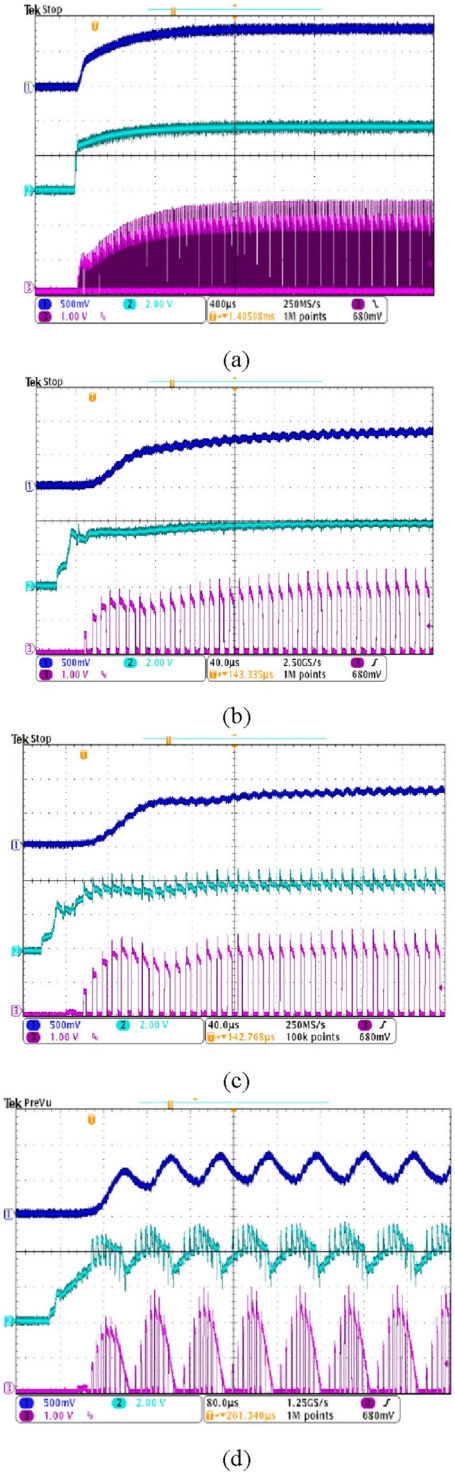

Figure 10. Start-up responses when the integral gain k_{ni} changes, (**a**) $k_{ni} \approx 0.0083\left(R_1^{'} = 12k\right)$, (**b**) $k_{ni} \approx 0.027(R_1^{'} = 3.7k)$, (**c**) $k_{ni} \approx 0.055\left(R_1^{'} = 1.8k\right)$, and (**d**) $k_{ni} \approx 0.1\left(R_1^{'} = 1k\right)$. Vertical scale: top traces-load current i_L(0.5 A/div.); middle traces-error amplifier output voltage COMP (2 V/div); bottom traces-transformer secondary output current i_o(1 A/div).

period becomes $\frac{1}{f_{osc}} = 8.2T_s \approx 82\mu$s, which is consistent with the measured unstable waveform as shown in Fig. 10d. The observed experimental results show excellent agreement with the root locus analysis. Figure 11 shows the simulated waveforms using the PSIM simulation program when the integral gain of the error amplifier

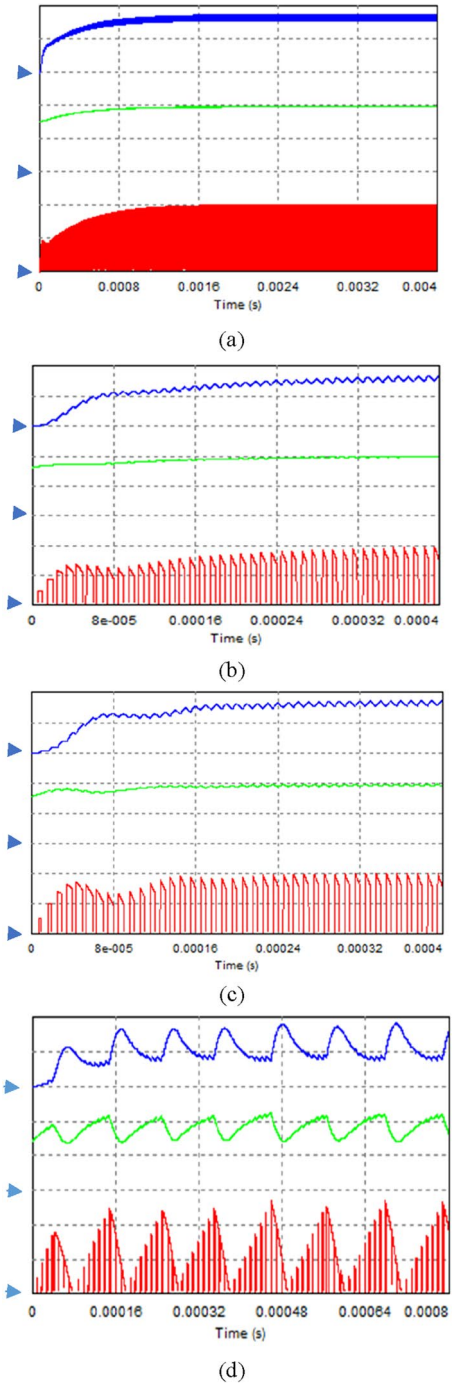

Figure 11. Simulated waveforms at start-up, (**a**) $k_{ni} \approx 0.0083\left(R_1^{'} = 12k\right)$, (**b**) $k_{ni} \approx 0.027(R_1^{'} = 3.7k)$, (**c**) $k_{ni} \approx 0.055\left(R_1^{'} = 1.8k\right)$, and (**d**) $k_{ni} \approx 0.1\left(R_1^{'} = 1k\right)$. Vertical scale: top traces-load current i_L(0.5 A/div.); middle traces-error amplifier output voltage COMP (2 V/div); bottom traces- transformer secondary output current i_o(1 A/div).

is changed. The soft start time simulation of the COMP signal is omitted. The experimental points of the two analysis planes are shown in Fig. 12. Comparison between the proposed design and the previous design[5] is shown in Table 2. The typical efficiency of this flyback LED driver with an output power of 25 W is over 90%.

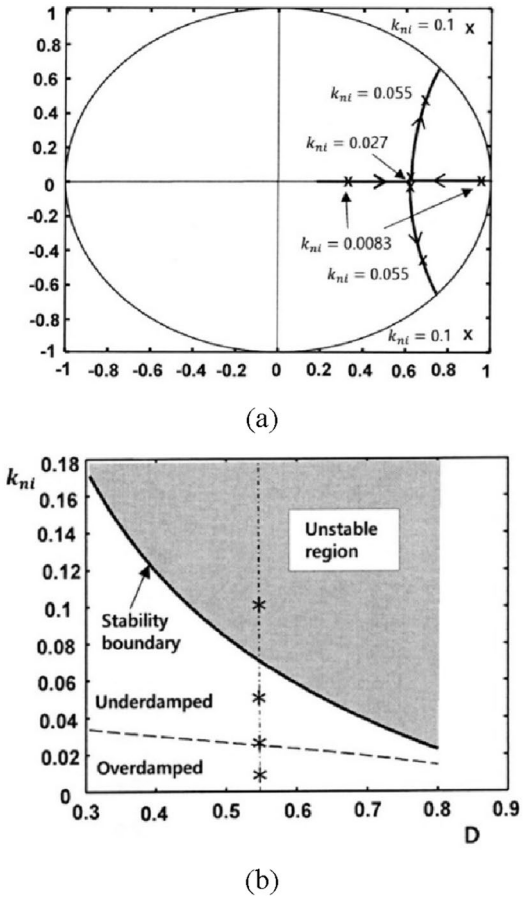

Figure 12. Experimental points: (**a**) pole locations in the z-plane and (**b**) representations in the k_{ni} versus D plane.

Proposed design	Previous design ref. [5]
Discrete time domain design	Continuous time domain design
Simultaneous error amplifier and current-loop designs	Error amplifier design after designing current loop
Constant slope compensation	Variable slope compensation
Internal ramp compensation signal OSC of CS3842 used for the current loop	External exponential ramp compensation signal used for the current loop
Simple hardware implementation: 3 resistors for the current loop, and 1 resistor and 1 capacitor for the error amplifier	Complex hardware implementation: 2 transistors, 2 diodes, 7 resistors and 3 capacitors for the current loop, and 1 opamp, 6 resistors and 3 capacitors for the error amplifier

Table 2. Comparison between proposed and previous current-mode controller designs.

Conclusion

A sequential process of modeling for a CMC flyback LED driver with a stabilizing ramp is proposed. Discrete time equations representing the behavior of the CMC flyback converter are derived. Then these equations are linearized with respect to the steady-state operating point. At the moment of switching, the control law is also linearized with respect to the operating point. In the next step, a linearized CMC flyback LED driver with a stabilizing ramp is derived by combining the two models of a linearized flyback converter and a linearized switching control law.

The inner feedback loop uses a current mode controller with ramp compensation slope. A PI compensator is used as an error amplifier in the output feedback loop. Here is a suggested step-by-step procedure for selecting feedback loop gains such as slope ratio and integral gain in the output feedback loop. First, S_{r0} is chosen to be 1 or a slightly greater value. Second, k_p is set to zero. The integral gain k_{ni} is designed to be close to the critical gain obtained using (17). Third, the maximum value of the comparator input voltage requires a limit[27]. To accommodate this, SF is calculated. This SF is less than 1. The actual integral gain k'_{ni} is calculated by multiplying k_{ni} by SF.

Using the step-by-step procedure described above, the design engineer can easily select the appropriate feedback gains for a well-characterized system. The proposed control can be implemented with a very simple compensation circuit. The validity of the proposed design is confirmed through the presented experimental results.

Data availability

All data generated or analysed during this study are included in this published article.

Received: 18 November 2022; Accepted: 7 April 2023
Published online: 18 April 2023

References

1. Molavi, N. & Farzanehfard, H. Load-independent hybrid resonant converter for automotive LED driver applications. *IEEE Trans. Power Electron.* **37**, 8199–8206 (2022).
2. Mukherjee, S., Yousefzadeh, V., Sepahvand, A., Doshi, M. & Maksimovic, D. A two-stage automotive LED driver with multiple outputs. *IEEE Trans. Power Electron.* **36**, 14175–14186 (2021).
3. Soares, G. M., Alonso, J. M. & Braga, H. A. C. Investigation of the active ripple compensation technique to reduce bulk capacitance in offline flyback-based LED drivers. *IEEE Trans. Power Electron.* **33**, 5206–5214 (2018).
4. He, Q., Luo, Q., Wei, Y. & Sun, P. A variable inductor controlled single-stage AC/DC converter for modular multi-channel LED driver. *IEEE Trans. Energy Convers.* **36**, 2912–2923 (2021).
5. Lamar, D. G. *et al.* Design-oriented analysis and performance evaluation of a low-cost high-brightness LED driver based on flyback power factor corrector. *IEEE Trans. Ind. Electron.* **60**, 2614–2626 (2013).
6. Li, H., Li, S. & Xiao, W. Single-phase LED driver with reduced power processing and power decoupling. *IEEE Trans. Power Electron.* **36**, 4540–4548 (2021).
7. Abdelmessih, G. Z., Alonso, J. M., Spode, N. D. & Dalla Costa, M. A. High-efficient electrolytic-capacitor-less offline LED driver with reduced power processing. *IEEE Trans. Power Electron.* **37**, 1804–1815 (2022).
8. Tian, H., Chen, M., Liang, G. & Xiao, X. Single-phase rectifier with reduced common-mode current, auto-PFC, and power decoupling ability. *IEEE Trans. Power Electron.* **37**, 6873–6882 (2022).
9. Cheng, H. L., Chang, Y. N., Chang, C. H., Hsieh, S. Y. & Cheng, C. A. A novel high-power-factor AC/DC LED driver with dual flyback converters. *IEEE J. Emerg. Sel. Top. Power Electron.* **7**, 555–564 (2019).
10. Kim, M. G. A study on optimal selection of inductance for power factor improvement of buck AC/DC LED Driver with wide input voltage range. *Trans. Korean Inst. Power Electron.* **26**, 302–305 (2021).
11. Lee, S. W. & Do, H. L. A single-switch AC-DC LED driver based on a boost-flyback PFC converter with lossless snubber. *IEEE Trans. Power Electron.* **32**, 1375–1384 (2017).
12. Zhang, X. *et al.* A soft-switching transformer-less step-down converter based on resonant current balance module. *IEEE Trans. Power Electron.* **36**, 8206–8218 (2021).
13. Liu, P. J., Hsu, Y. C. & Hsu, S. R. Drain-voltage balance and phase-shifted PWM control schemes for high-efficiency parallel-string dimmable LED drivers. *IEEE Trans. Ind. Electron.* **65**, 6168–6176 (2018).
14. Liu, X. *et al.* Buck-boost-buck-type single-switch multistring resonant LED driver with high power factor and passive current balancing. *IEEE Trans. Power Electron.* **35**, 5132–5143 (2020).
15. Middlebrook, R. D. Modeling current-programmed buck and boost regulators. *IEEE Trans. Power Electron.* **4**, 36–52 (1989).
16. Lee, F. C., Iwens, R. P., Yu, Y. & Triner, J. E. Generalized computer-aided discrete-time modeling and analysis of dc-dc converters. *IEEE Trans. Industr. Electron. Contr. Instrum.* **26**, 58–69 (1979).
17. Jung, Y. S. & Kim, M. G. Time-delay effects on DC characteristics of peak current controlled power LED driver. *J. Power Electron.* **12**, 715–722 (2012).
18. Feng, W., Lee, F. C. & Mattavelli, P. Optimal trajectory control of LLC resonant converter for LED PWM dimming. *IEEE Trans. Power Electron.* **29**, 979–987 (2014).
19. Kim, M. G. Proportional-Integral (PI) compensator design of duty-cycle-controlled buck LED driver. *IEEE Trans. Power Electron.* **30**, 3852–3859 (2015).
20. Kim, M. G. High-performance current-mode-controller design of buck LED driver with slope compensation. *IEEE Trans. Power Electron.* **33**, 641–649 (2018).
21. Menke, M. F., Seidel, A. R. & Tambara, R. V. LLC LED driver small-signal modeling and digital control design for active ripple compensation. *IEEE Trans. Ind. Electron.* **66**, 387–396 (2019).
22. Verghese, G. C., Elbuluk, M. E. & Kassakian, J. G. A general approach to sampled-data modeling for power electronic circuit. *IEEE Trans. Power Electron.* **1**, 76–89 (1986).
23. Kim, M. G. & Youn, M. J. A discrete time domain modeling and analysis of controlled series resonant converter. *IEEE Trans. Ind. Electron.* **38**, 32–40 (1991).
24. Kim, M. G. & Youn, M. J. An energy feedback control of series resonant converter. *IEEE Trans. Power Electron.* **6**, 338–345 (1991).
25. Kim, M. G., Lee, D. S. & Youn, M. J. A new state feedback control of resonant converters. *IEEE Trans. Ind. Electron.* **38**, 173–179 (1991).
26. Huber, L., Gang, L. & Jovanovic, M. M. Design-oriented analysis and performance evaluation of buck PFC front end. *IEEE Trans. Power Electron.* **25**, 85–94 (2010).
27. Cherry Semiconductor Corp, CS3842B datasheet. http://www.onsemi.com/pub/Collateral/CS3842B-D.PDF (2001).
28. Phillips, C. L. & Nagle, H. T. Jr. *Digital Control System Analysis and Design* (Prentics-Hall, 1984).

Acknowledgements

This work was supported by a Research Grant of Pukyong National University (2021)

Author contributions

M.G.K. wrote the manuscript, and performed the modeling, analysis, design, and experiment.

Competing interests

The author declare no competing interests.

Additional information

Correspondence and requests for materials should be addressed to M.-G.K.

Reprints and permissions information is available at www.nature.com/reprints.

Publisher's note Springer Nature remains neutral with regard to jurisdictional claims in published maps and institutional affiliations.

Open Access This article is licensed under a Creative Commons Attribution 4.0 International License, which permits use, sharing, adaptation, distribution and reproduction in any medium or format, as long as you give appropriate credit to the original author(s) and the source, provide a link to the Creative Commons licence, and indicate if changes were made. The images or other third party material in this article are included in the article's Creative Commons licence, unless indicated otherwise in a credit line to the material. If material is not included in the article's Creative Commons licence and your intended use is not permitted by statutory regulation or exceeds the permitted use, you will need to obtain permission directly from the copyright holder. To view a copy of this licence, visit http://creativecommons.org/licenses/by/4.0/.

© The Author(s) 2023